Slab Rollback Orogeny model for the evolution of the Central Alps: Seismo-Thermo-Mechanical test

Luca Dal Zilio [1,2*], Edi Kissling [1], Taras Gerya [1] & Ylona van Dinther [3]

[1] *Mechanical Engineering Department, California Institute of Technology, Pasadena, California, USA*

[2] *Institute of Geophysics, ETH Zürich, Sonneggstrasse 5, 8092 Zürich, Switzerland*

[3] *Department of Earth Sciences, Utrecht University, The Netherlands*

** Corresponding author e-mail: dalzilio@caltech.edu*

Abstract

The role of mantle-lithosphere interactions in shaping mountain belts has long been debated. Several conceptual models implicate a key role for horizontal kinematic forces in sustaining mountain building processes. For the central European Alps, however, recent stratigraphic, palaeo-altimetry and lithosphere structural evidence suggest that dynamic vertical forces — provided by a *Slab Rollback Orogeny* (SRO) model — are the primary determinant of the latest construction of thick nappe successions, the large-scale tectonic evolution, and the present-day seismicity pattern. In this study we investigate this hypothesis by performing 2-D, high-resolution, rheologically consistent, visco-elasto-plastic seismo-thermo-mechanical numerical modeling, which simulates both tectonic and seismic processes in a subduction and continental collision setting. Our numerical experiments reproduce the self-driven stages of oceanic subduction, continent-continent collision, and spontaneous slab breakoff. The subsequent evolution of the orogen shows how slow, but persistent, flexural bending of post-collisional residual slab and crustal delamination control the latest evolution of the orogen. Bending-related slab suction leads to the coeval development of nappe stacking of the buoyant crustal root, widening of the orogen, and a distinctive seismicity pattern that implies the occurrence of extensional forces at work in the orogen and beneath the foreland basin. Our results thus suggest that a self-sustaining rollback mechanism is capable of explaining the post-collisional evolution of the Central Alps, including the construction of thick sedimentary successions in the Molasse foreland basin and the most recent tectonic deformation of the Jura fold-and-thrust belt.

1. Introduction

The process of continent–continent collision in shaping mountain ranges and adjacent foreland basins has been discussed over many decades (e.g., Malinverno & Ryan, 1986; Beaumont *et al.* , 1996; Avouac, 2015a). According to most commonly used concept, the evolution of mountain belts has largely been driven by the horizontal convergence between the two colliding plates (e.g., Schmid *et al.* , 1996; Handy *et al.* , 2010). This view is based on the perception in which a rigid indenter — frequently exemplified by a bulldozer — converts the kinematic convergence into the

mountain building processes (Willett, 2010). For the central European Alps (Fig. 1A), however, this general concept is neither consistent with observations nor with isostatic mass balancing models (Schlunegger & Kissling, 2015).

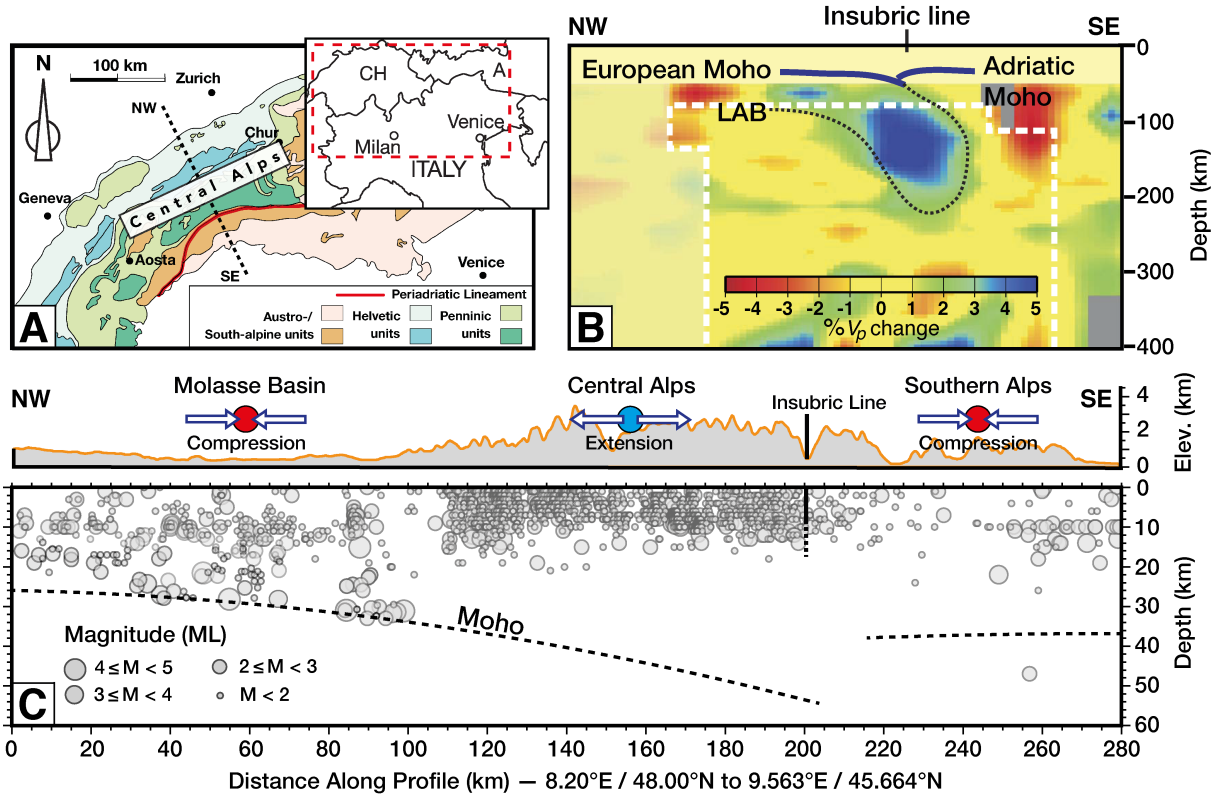

Figure 1: **A**: Inset map illustrating the Alps and its foreland basin along with the section discussed in this paper. **B**: Teleseismic tomography cross-section illustrating European slab geometry beneath the central Alps. The figure shows lateral variations of P-wave velocity Vp beneath the Moho. **C**: Topographic signal and vertical cross-section approximately perpendicular to the strike of the Central Alps. Transparent gray circles represent hypocenters. Dashed black lines indicate the Moho with a minimum ±3 km uncertainty of the depth.

The crustal root has been seismically determined to be ∼60-km thick, and thus far out of conventional Airy-isostatic equilibrium with a mean surface topography of only about 2 km (Kissling, 1993). A more recent, alternative explanation suggests that the Central Alpine evolved in response to a slab rollback process, in which the dynamic vertical forces of a retreating subduction and crustal buoyancy forces are the major driving mechanisms of the orogenic system (Brun & Faccenna, 2008; Kissling & Schlunegger, 2018). This revised model on Alpine evolution, which we refer to as *Slab Rollback Orogeny* (SRO) model, consider the well-known concepts of slab pull and retreat, force balancing, and the principles of mass conservations. This SRO model provides a dynamically consistent mechanism to explain the construction of thick sedimentary successions in the Molasse basin where the extra slab load has maintained the Alpine surface at moderate, but persistent, elevations (Schlunegger & Kissling, 2015). This SRO model provides a dynamically consistent mechanism to explain the construction of thick sedimentary successions in the Molasse basin (Schlunegger & Kissling, 2015) and the imbricate stacking of the crustal root (Fry *et al.* , 2010).

On a large-scale, teleseismic tomography cross-sections have shown that, along the NW–SE transect across the Central Alps, the slab dips with only $\sim$60° (Fig. 1B), while along a N–S transect at $\sim$10°E longitude the slab hangs in a sub-vertical position beneath the core of the Alps (Lippitsch *et al.* , 2003). Geological interpretations based on receiver function profile (Zhao *et al.* , 2015) and on teleseismic imaging (Zhao *et al.* , 2016) argue that the European mantle slab is still attached beneath southern Western Alps. In contrast, recent teleseismic full-waveform inversion by Beller *et al.* (2017) indicates a low-velocity zone in the lower lithosphere and they explicitly support the hypothesis of a slab tearing beneath the Western Alpine arc.

If the scenario proposed by Lippitsch *et al.* (2003) is correct, the SRO model provides a possible explanation for the current seismicity pattern across the Central Alps (Fig. 1C), which is characterized by bending-related faulting events beneath the Molasse Basin and within the subducting European plate (Singer *et al.* , 2014). This post-collisional slab rollback orogeny scenario thus suggests a mechanism where tectonic processes related to a retreating collision regime conditioned the subduction processes, the accommodation of space in the Molasse Basin and the crustal accretion in the adjacent Alps. However, although well established, this new theory has never been tested through the use of physics-based numerical methods.

In this study, we employ a newly-developed, high-resolution (400 m), 2-D Seismo-Thermo-Mechanical (STM) model to simulate both the long-term tectonic of collisional orogens and the short-term seismicity (e.g., Dal Zilio *et al.* , 2018b) and to test whether the buoyancy forces of the postulated post-collisional rollback are sufficient to drive the evolution and to shape the Central Alps as we know them today.

2. Methods

2.1. ***Numerical code description***

In order to simulate the dynamics of mountain building processes coupled to mantle dynamics, we employ the seismo-thermo-mechanical (STM) (van Dinther *et al.* , 2013). This numerical code solves for the two-dimensional steady state momentum equations and heat conservation equation using the finite-difference/marker-in-cell method on a Eulerian grid Gerya & Yuen (2007):

$$\frac{\partial v_x}{\partial x} + \frac{\partial v_z}{\partial z} = 0 \tag{1}$$

$$\frac{\partial \sigma'_{xx}}{\partial x} + \frac{\partial \sigma'_{xz}}{\partial z} - \frac{\partial P}{\partial x} = \rho \frac{Dv_x}{Dt} \tag{2}$$

$$\frac{\partial \sigma'_{zz}}{\partial z} + \frac{\partial \sigma'_{zx}}{\partial x} - \frac{\partial P}{\partial z} = \rho \frac{Dv_z}{Dt} - \rho g \tag{3}$$

These equations are solved to obtain the horizontal and vertical velocities (v_x and v_z) and pressure (P, defined as the mean stress), whereas ρ is density, σ'_{ij} are deviatoric stress tensor components,

and g = 9.81 m/s^2 is the vertical component of the gravitation acceleration. The advection of transport properties including viscosity, plastic strain and temperature is performed with the displacement of Lagrangian markers.

The momentum equations include the inertial term to stabilize higher slip rates at low time steps. A time step of 1 year, however, reduces our formulation to a virtually quasi-static one. Ruptures during the resulting events hence represent the occurrence of rapid threshold-exceeding slip during which permanent displacement and stress drop occur along a localized interface.

The heat equation describes the balance of heat in a continuous medium and is solved in a Lagrangian manner and is expressed in the following way (Gerya, 2010):

$$\rho C_p \frac{DT}{Dt} = -\frac{\partial q_x}{\partial x} - \frac{\partial q_z}{\partial z} + H_\mathrm{r} + H_\mathrm{a} + H_\mathrm{s}; \tag{4}$$

$$q_x = -k(T,C)\frac{\partial T}{\partial x}; \tag{5}$$

$$q_z = -k(T,C)\frac{\partial T}{\partial z}; \tag{6}$$

$$H_a = T\alpha\frac{DP}{Dt} \tag{7}$$

$$H_\mathrm{s} = \sigma'_{ij}\ \dot{\varepsilon}_{ij,\ vp}; \tag{8}$$

Such a formulation takes into account the effect of radioactive heating (H_r), adiabatic heat production/consumption (H_a), and shear heating (H_s). DP/Dt represents the substantive time derivative of pressure, whereas α is the thermal expansion. Thermal conductivity $k(T,C)$ is a function of both temperature and composition (cf. Table 1). q_x and q_z are the horizontal and vertical components of the heat flux vector, $\dot{\varepsilon}_{ij,\ vp}$ is the visco-plastic component of the deviatoric strain rate tensor, and H is the rock enthalpy. The isobaric heat capacity (C_p) and isothermal compression term are computed at each timestep and takes into account the effect of latent heat due to phase transformations (Faccenda & Dal Zilio, 2017). Evaluation of H_T and H_s terms requires information from the pressure and stress tensor components. These terms are thus computed after solving the Stokes equations. The heat equation can then be solved taking into account the effect of isothermal compression, phases changes and shear heating at the current timestep.

2.2. ***Rheological model***

We consider that the strength of the lithosphere is controlled, at the different timescales of orogeny, by the combination of both brittle and ductile deformation mechanisms in a visco-elasto-plastic rheology. Viscous creep is computed in terms of deformation invariants and depends on strain rate, temperature, and pressure (Ranalli, 1995). The effective viscosity (η_{eff}) of the deformation is calculated as a combination of diffusion (η_{diff}) and dislocation creep (η_{dis}):

$$\frac{1}{\eta_{eff}} = \frac{1}{\eta_{diff}} + \frac{1}{\eta_{disl}} \tag{9}$$

$Material$ $flow\ law$ [a]	ρ_0 [b] ($kg\,m^{-3}$)	E_a [a] ($kJ\,mol^{-1}$)	V_a [a] (J/bar)	n [a]	η_0 [a] ($Pa^n\,s$)	Hr [b,c] (μWm^{-3})	k [a] $Wm^{-1}K^{-1}$	G (GPa)	μ_s [d,e,f]	λ [g,h]
Sediments (Wet Qz)	2600	154	1.2	2.3	1.97 x 10^{17}	1.5	$[0.64 + 807/(T + 77)]$ $exp(4\ 10^{-5}P)$	25	0.35	0.4
Upper cont. crust (Wet Qz)	2750	154	0.8	2.3	1.97 x 10^{17}	0.25	$[0.64 + 807/(T + 77)]$ $exp(4\ 10^{-5}P)$	34	0.6	0.4
Lower cont. crust (Mafic Granulite)	3000	445	0.8	4.2	1.25 x 10^{21}	1.5	$[0.64 + 807/(T + 77)]$ $exp(4\ 10^{-5}P)$	34	0.6	0.4
Upper oc. crust (Wet Qz)	3000	154	0.8	2.3	1.97 x 10^{17}	0.25	$[1.18 + 974/(T + 77)]$ $exp(4\ 10^{-5}P)$	38	0.6	0.95
Lower oc. crust (Plg-An 75%)	3300	238	0.8	3.2	4.8 x 10^{22}	0.0022	$[1.18 + 974/(T + 77)]$ $exp(4\ 10^{-5}P)$	38	0.6	0.4
Mantle (Dry Olivine)	3300	532	0.8	3.5	3.98 x 10^{16}	0.0022	$[0.73 + 1293/(T + 77)]$ $exp(4\ 10^{-5}P)$	67	0.6	0.4

Table 1: Rheological parameters. ρ_0 is the reference density, E_a is the activation energy, V_a is the activation volume, n is the stress exponent, η_0 is the reference viscosity, Hr is the radiogenic heat production, G is the shear modulus, μ_s is the static friction coefficient and λ is the pore-fluid pressure factor (P_{fluid}/P_{solid}). Other properties for all rock types: cohesion (C) is 1 MPa (Schultz, 1995), specific heat capacity (C_p) is 1000 $J\ kg^{-1}K^{-1}$, thermal conductivity (k) is in $Wm^{-1}K^{-1}$ at T_K and P_{MPa}, thermal expansion α_ρ= 3x10^{-5} K^{-1} and compressibility β_ρ=1x10^{-5} MPa^{-1}. [a] Ranalli (1995); [b] Turcotte & Schubert (2002); [c] Rudnick & Fountain (1995); [d] Di Toro *et al.* (2011); [e] Del Gaudio *et al.* (2009); [f] Den Hartog *et al.* (2012); [g] Sibson (1994); [h] Seno (2009).

The calculation of the viscosity associated with dislocation creep regime is formulated as follows:

$$\eta_{disl} = \frac{1}{2}\, A_d\, \sigma\prime_{II}^{1-n}\, exp(\frac{E_a + PV_a}{nRT}) \tag{10}$$

where $\sigma\prime_{II}$ is the second invariant of deviatoric stress tensor, A_d is the pre-exponential factor, E_a the activation energy, V_a is the activation volume, n the stress exponent, and R is the gas constant. Those material properties are determined from laboratory flow experiments and are given in Table 1.

Dislocation creep is dominant for high stress levels, while diffusion creep is a thermally activated mechanism and is the most convenient way to accommodate deformation at low stress conditions:

$$\eta_{diff} = \frac{1}{2}\, A_d\, \tau_{tr}^{1-n}\, exp(\frac{E_a + PV_a}{nRT}). \tag{11}$$

In this case, τ_{tr} defines the stress transition between diffusion creep and dislocation creep, which is assumed to occur at 30 kPa (Turcotte & Schubert, 2002).

Our rheological model takes into account a second semi-brittle deformation mechanism characterized by the exponential flow of olivine and also known as Peierls mechanism. As demonstrated in Duretz *et al.* (2011), Peierls creep in olivine is a key mechanism for slab breakoff, generally causing slabs to break earlier and at shallower depths. This flow mechanism has been put in evidence in a number experimental studies (Evans & Goetze, 1979; Katayama & Karato, 2008). Moreover, recent studies have shown that the existence of plate tectonics requires sufficiently lithospheric yield stress that are lower than Mohr–Coulomb stresses (Van Heck & Tackley, 2008). Such conditions necessitate the use of stress limiters such as Peierls creep which promotes the localization of deformation in the lithospheric mantle (Kameyama *et al.* , 1999; Lu *et al.* , 2011). The effective viscosity corresponding to the Peierls creep regime is characterized by an exponential dependance on the second stress invariant and is formulated as:

$$\eta_{peierls} = \frac{1}{2A_{peierls}\sigma_{II}} exp\left(\frac{E_a + PV_a}{nRT}\left(1 - \left(\frac{\sigma_{II}}{\sigma_{peierls}}\right)^p\right)^q\right) \; ; \tag{12}$$

for dry olivine, $A_{peierls} = 10^{7.8}\, 10^{-12}\; Pa^{-2}s^{-1}$ is the material constant for Peierls creep, $\sigma_{peierls}$ is the Peierls stress that limits the strength of the material and corresponds to 9.1 GPa (Evans & Goetze, 1979). Exponents p and q depend on the shape and geometry of obstacles that limit the dislocation motion and are equal to 1 and 2, respectively. The Peierls mechanism is a dominant deformation mechanism of the downgoing slab, where the temperature is low and stress is high (e.g. Karato *et al.* , 2001).

The 2-D steady state momentum equations are solved using constitutive relations that relate deviatoric stresses and strain rates in a nonlinear visco-elasto-plastic manner:

$$\dot{\varepsilon_{ij}} = \frac{1}{2G}\frac{D\sigma'_{ij}}{Dt} + \frac{1}{2\eta}\sigma'_{ij} + \begin{cases} 0 & \text{for } \sigma'_{II} < \sigma_{yield} \\ \chi\frac{\partial\sigma'_{II}}{\partial\sigma'_{ij}} = \chi\frac{\partial\sigma'_{ij}}{2\sigma'_{II}} & \text{for } \sigma'_{II} = \sigma_{yield} \end{cases} \tag{13}$$

where G is shear modulus and η is effective viscosity. $D\sigma'_{ij}/Dt$ is the objective co-rotational time derivative solved using a time explicit scheme (Gerya, 2010) and $\sigma_{II} = \sqrt{{\sigma'_{xx}}^2 + {\sigma'_{xz}}^2}$ is the second invariant of the deviatoric stress tensor, and χ is a plastic multiplier connecting plastic strain rates and stresses. Introducing a visco-plastic viscosity (η_{vp}), we can rewrite equation 13 as:

$$\sigma'_{ij} = 2\eta_{vp} Z \dot{\varepsilon_{ij}} + \sigma_{ij}(1 - Z) \tag{14}$$

where Z is the visco-elasticity factor:

$$Z = \frac{G\Delta t_{comp}}{G\Delta t_{comp} + \eta_{vp}} \tag{15}$$

where Δt_{comp} is the computational time step.

The brittle part of the lithosphere is controlled by Mohr–Coulomb (or non-associative Drucker-Prager) plasticity which expresses the linear dependence of the geomaterials resistance on the total pressure Prager & Drucker (1952). Mohr–Coulomb plasticity acts as a stress limiter in the regions where the second stress invariant (σ_{ii}) exceeds the material yield stress. The yield stress depends on the pressure, the standard strength (i.e., cohesion) C (MPa), and the effective friction coefficient μ_{eff}:

$$\sigma_{yield} = C + \mu_{eff}\, P \tag{16}$$

where C is the cohesion.

An important component in the yield criterion is the friction coefficient. Following the approach of van Dinther *et al.* (2013), we apply a strongly rate-dependent friction formulation (Ampuero & Ben-Zion, 2008), in which the effective friction coefficient μ_{eff} depends on the visco-plastic slip velocity $V = (\sigma_{yield}/\eta_m)\Delta x$, in which η_m is the local viscosity from the previous time step and Δx is the Eulerian grid size:

$$\mu_{eff} = \frac{V_c\, \mu_s \; + \; V\, \mu_d}{V_c + V} \tag{17}$$

$$\gamma = 1 - (\mu_d/\mu_s) \tag{18}$$

where μ_s and μ_d are static and dynamic friction coefficients, respectively, V_c is the characteristic velocity, namely the velocity at which half of the friction change has occurred, and γ represents the amount of slip velocity-induced weakening if $\gamma = 1 - (\mu_d/\mu_s)$ is positive, or strengthening if γ is negative.

When plastic yielding condition is locally reached we require a constant second invariant of deviatoric stresses (assuming the absence of elastic deformation)

$$\text{if} \quad \sigma'_{II} = \sigma_{yield} : \left\{ \quad \frac{D\sigma'_{II}}{Dt} = 0, \quad \dot{\varepsilon_{ij}}^{elastic} = 0 \right\}; \tag{19}$$

then the stress components are similarly (i.e., isotropically) corrected so that

$$\sigma'_{ij} = \sigma'_{ij} \cdot \frac{\sigma_{yield}}{\sigma'_{II}}. \tag{20}$$

Accordingly, the local viscosity-like parameter η_{vp} decreases to weaken the material and to localise deformation

$$\eta_{vp} = \eta \frac{\sigma'_{II}}{\eta\chi + \sigma'_{II}} \tag{21}$$

where

$$\chi = 2(\dot{\varepsilon_{II}} - \dot{\varepsilon_{II}}^{viscous}) = 2(\dot{\varepsilon_{II}} - \frac{1}{2\eta}\sigma'_{II}) \tag{22}$$

and

$$\dot{\varepsilon_{II}} = \sqrt{\dot{\varepsilon_{xx}}^2 + \dot{\varepsilon_{xz}}^2} \tag{23}$$

Finally the visco-plastic viscosity η_{vp} is corrected during plastic deformation:

$$\eta_{vp} = \frac{\sigma_{yield}}{2\dot{\varepsilon_{II}}} \tag{24}$$

On the other hand, if the plastic yielding condition is not satisfied, this means that the material is under elastic and/or viscous deformation (i.e., diffusion and/or dislocation creep), therefore $\eta_{vp} = \eta$.

2.3. ***Eclogitization***

Eclogitization of the continental mafic crust can have major effects on the evolution of continental plates. With the progression of the reaction, the eclogitized continental root becomes denser than the surrounding mantle and thus it is prone to foundering (Kay & Kay, 1993). Numerical models predict that high-density eclogite affects the orogeny evolution (Doin & Henry, 2001; Li *et al.* , 2016) and, if sufficiently weak, can lead to delamination of the continental plate (Krystopowicz & Currie, 2013).

Therefore, eclogitization of subducted crust is here implemented in a relatively simplified manner (Faccenda & Dal Zilio, 2017). More specifically, for the basalts of the upper and lower mafic crust, a phase transition from basalt to garnet-granulite and then eclogite (Ito & Kennedy, 1971) is applied. Eclogitization of the crust is implemented as a linear density increase with pressure and

temperature from 0% to 16% in the P–T region between the experimentally determined garnet-in and plagioclase-out phase transitions in basalt (Ito & Kennedy, 1971). For temperatures lower than $T_{ecl_{min}}$ = 673K no eclogitization is possible. For temperatures between $T_{ecl_{min}}$ and $T_{ecl_{max}}$= 873 K the maximum density increase due to eclogitization is linearly increasing with temperature from 0% to 16%.

2.4. ***Estimation of Moment Magnitude (M_W)***

During the seismic cycle simulation we analyze all rupture events to determine their downdip rupture width (W). These events occurring throughout the orogen are recognized using a Rupture Detector Algorithm (RDA), which analyzes each Lagrangian marker in space and time throughout the simulation. If its velocity exceeds a threshold of 9.0 x 10^{-9} m s^{-1}, while simultaneously stresses drop more than 0.4 MPa that marker's physical properties are stored in a synthetic data set. Subsequently markers are grouped into one event when they occur within 400 m of a marker that ruptured this or the previous time step. The rationale for choosing these thresholds comes from the minimally common stress drop (Allmann & Shearer, 2009) and our Eulerian grid size of 400 m, respectively.

From these spontaneous rupture paths we measure the rupture width (W) to estimate the moment magnitude (M_W) using the empirical scaling relations in Wells & Coppersmith (1994). This empirical relationship is available from regression analysis based on a large numbers of events in nature:

$$M_W \; = \; a \; + \; b \, log \, (W), \tag{25}$$

where a and b are coefficients that vary with the style-of-faulting (i.e., normal or reverse faulting). We chose Wells & Coppersmith (1994) because they include various types of faulting and different tectonic environments.

2.5. ***Setup***

The initial model domain consists of two continental plates separated by an oceanic basin (see Fig. 2A). The dimensions of the model box is 3000 x 1200 km^2 (1921 x 347 nodes), and all the mechanical boundaries are free slip. Variable grid spacing enables to reach a 400 m grid resolution in the central part of the domain where the continental collision takes place. Lithological structure are resolved with $\sim$33 million markers. In order to study the interplay between subduction and orogenic evolution, we follow the semi-dynamic approach employed in Duretz *et al.* (2011). The initial conditions of the model are built during the initial stage of kinematic convergence. During this period, the oceanic subduction is kinematically prescribed using internal kinematic constrains (5 cm/yr until 200 km of convergence is accommodated). With ongoing convergence, the upper plate decouple from the lateral sides of the box; this zones accommodate hot mantle upwellings and are therefore the location where oceanic ridges spontaneously develop. After this model initialization step, the internal kinematic constrain is removed and the model is driven by internal, buoyancy forces. Thus, the obtained thermo-mechanical state is employed as the initial condition for a self-driven, retreating subduction and continental collision. The subduction and collision rates, which are not in steady state, are controlled by the contribution of slab pull, crustal buoyancy, and dissipative

forces. We employ an additional 20 km thick layer of sticky air (η_{air} = 10^{18} Pa s, ρ_{air} = 1 kg/m^3) in order to mimic the effect of a free surface and enable the development of topography (Crameri *et al.* , 2012).

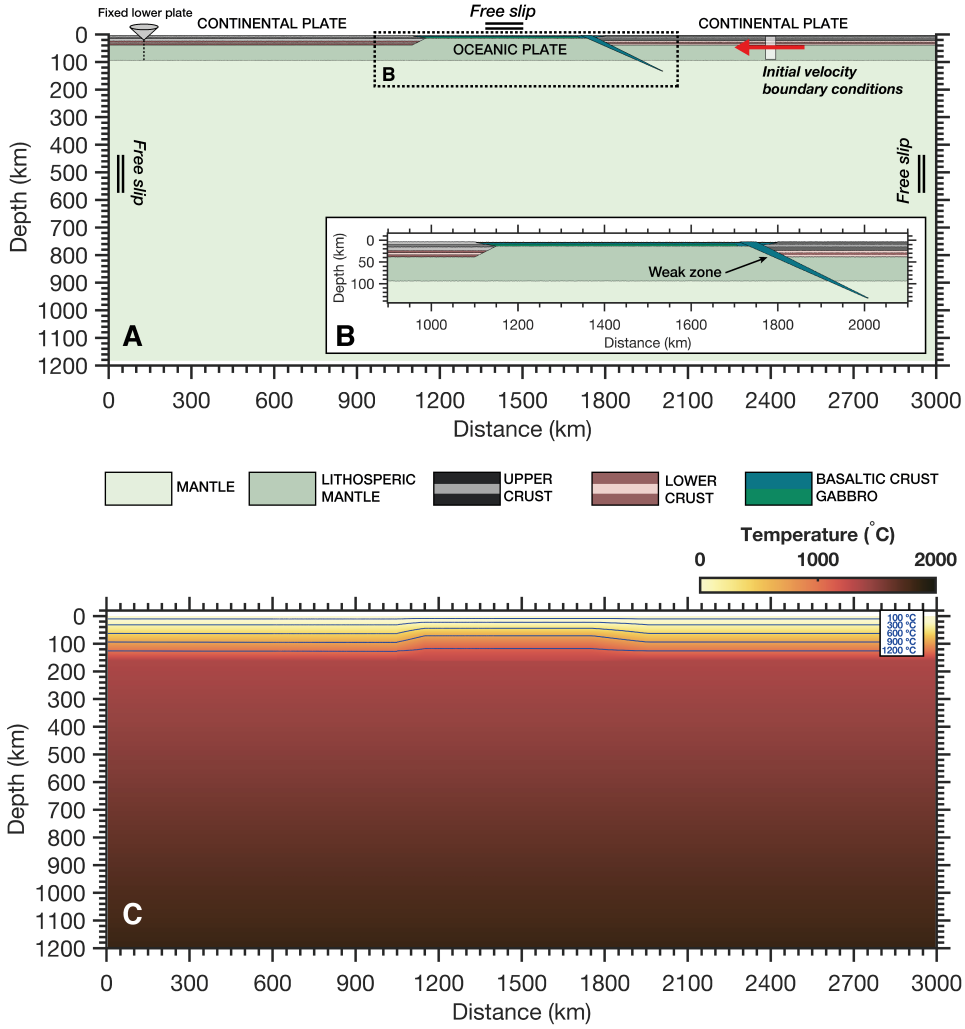

Figure 2: 2-D initial setup. **A**: Initial composition map including boundary conditions. **B**: Zoom of oceanic plate and pre-imposed weak zone to initiate subduction. Using a similar approach of Duretz *et al.* (2011), the model simulates subduction initiation through the use of a fixed convergence rate on the upper plate until ∼200 km of oceanic crust has been subducted. Plate convergence rate is applied at 2500 km on the right (upper) plate (red arrow). **C**: Initial temperature distribution.

The thermal structure of the oceanic lithosphere was calculated from the half space cooling model for a given plate age (Turcotte & Schubert, 2002) using a slab age of 70 Ma and a diffusivity of 10^{-6} m^2 s^1. The initial continental geotherm is defined as a linear temperature variation from the model surface (T=293 K) to the lithosphere–asthenosphere boundary (T=1617.6 K), the left and right sides of the model domain are insulating boundaries. The geothermal gradient in the asthenospheric mantle below the lithosphere is 0.5 K/km (Fig. 2C).

In order to initiate subduction a weak zone was imposed on the right ocean–upper plate tran-

sition. The weak zone cuts through the whole lithospheric mantle with an angle of $\sim 30^{\circ}$ and is characterized by weak plastic strength (1 MPa) and wet olivine rheology (Ranalli, 1995). Despite the fact that subduction initiation can be modelled in a geologically more relevant manner (e.g., Nikolaeva *et al.* , 2010), the use of such a weak zone remains useful for our specific setup.

3. Numerical Model Results

After a stage of pre-imposed model initiation, subduction and subsequent collision are solely driven by the buoyancy of the lithosphere slab. The upper Adriatic plate is decoupled from Africa (e.g., Platt *et al.* , 1989) and free to move, whereas the lower plate is fixed to the left boundary. This setup is thus consistent with palaeomagnetic evidence that the lower (European) continental plate has remained nearly stationary since the Late Cretaceous (Dewey *et al.* , 1989).

3.1. ***Rollback subduction, collision, and slab breakoff***

After an initial stage of kinematically imposed subduction initiation, oceanic lithosphere sinks spontaneously at the ocean-upper plate (Adria) continental margin. Self-sustaining retreating subduction occurs in all our simulations: slab rollback causes the migration of the trench and exerts a suction force to the overriding plate, while the subduction-induced mantle flow maintains the upper plate highly coupled with the retreating slab (Fig. 3) (e.g., Faccenda *et al.* , 2009; Dal Zilio *et al.* , 2018a; Dal Zilio, 2018).

Slab necking occurs at a relatively shallow depth of approximately 250 km during the stage of slab steepening. Breakoff occurs at the ocean–continent transition a few million years after the collision stage initiated (Fig. 4). Slab breakoff and subsequent rebound produces a sharp topographic signal, with an exhumation of $\sim$5 km recorded above the orogen. Such exhumation, defined as the total displacement of rocks with respect to the surface, is thus controlled by the rate of erosion and the rate of removal of overburden by tectonic processes. The topographic response is relatively rapid ($\sim$5 My) and produces an average uplift rate of 0.8 mm/yr, predominantly above the lower continental plate, and consistent with the observations (Schlunegger & Kissling, 2015).

3.2. ***Post slab breakoff evolution of the orogen***

Our numerical experiments indicate that the removal of the oceanic lithospheric load during slab breakoff is responsible for a stress redistribution within the lithosphere. Release of the gravitational stresses during breakoff is followed by the unbending of the remaining slab and a localized increase of stress in the lower plate related to the positive buoyancy of the subducted continental crust. However, our numerical simulations show that the vertical slab pull force — offered by the remaining slab — remains the dominant driving force in the collisional system (Fig. 5).

Following the rapid transient visco-elastic rebound (Gerya *et al.* , 2004; Duretz *et al.* , 2011), the resulting flexural bending provokes the migration of the whole orogen towards the foreland basin (Fig. 6). The ongoing rollback collision triggers crustal delamination, shortening at shallower crustal levels, and uplift of the frontal part of the orogen and in the foreland basin. At deeper crustal levels, extrusion and stacking of buoyant crustal materials occur on the downgoing plate, while the remaining slab continues to subduct at a low, but detectable, sinking rate (Fig. 5). In addition, heating of

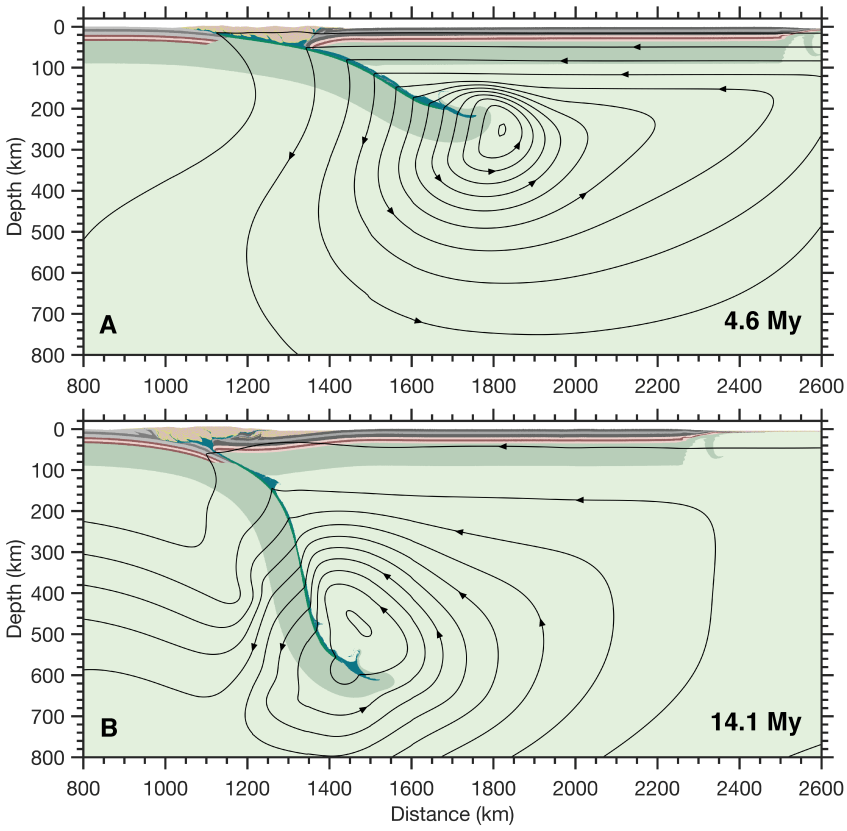

Figure 3: Thermomechanical evolution of a spontaneously bending oceanic plate and evolution at key stages of mantle-lithosphere interaction. Composition of the reference model after 4.6 My (**A**) and 14.1 My (**B**). The superimposed stream function display the effect of subduction-induced trench suction and return flow in mantle, which maintain the upper plate coupled with the retreating slab.

the slab decreases the flexural strength and increases the curvature of the subducted plate, thus inducing large-scale extension.

The final convergence rate is relatively small (2–3 mm/yr; Fig. 7), in agreement with continuous GPS measurements (Calais *et al.* , 2002). The uplift rate is $\sim$0.6 mm/yr in the core of the orogen and $\sim$0.2–0.3 mm/yr in the foreland basin, with an average exhumation of 2 km in 10 My, thus confirming analyzes of Alpine thermo-chronometric ages (Fox *et al.* , 2015). The orogenic volume is mostly accommodated on the lower continental plate, with a maximum topography greater than 5 km in height. Finally, at *ca.* 20 Myr after slab breakoff, crustal shortening and rock uplift propagate through the continental interiors, similarly to the main shortening observed in the Jura thrust belt over the last 10 Ma (e.g., Burkhard, 1990), thus resulting in a widening of the orogenic belt above the lower continental plate. Interestingly, our numerical experiments suggest that, when the post breakoff remaining slab tip is less than 160 km deep, the vertical slab pull force decreases significantly.

3.3. ***Regional stresses and seismicity distribution***

The seismic cycle simulation shows a wide domain subjected to brittle faulting (Fig. 8). Seismogenic deformation in the orogenic wedge is largely driven by extensional stresses resulting from the

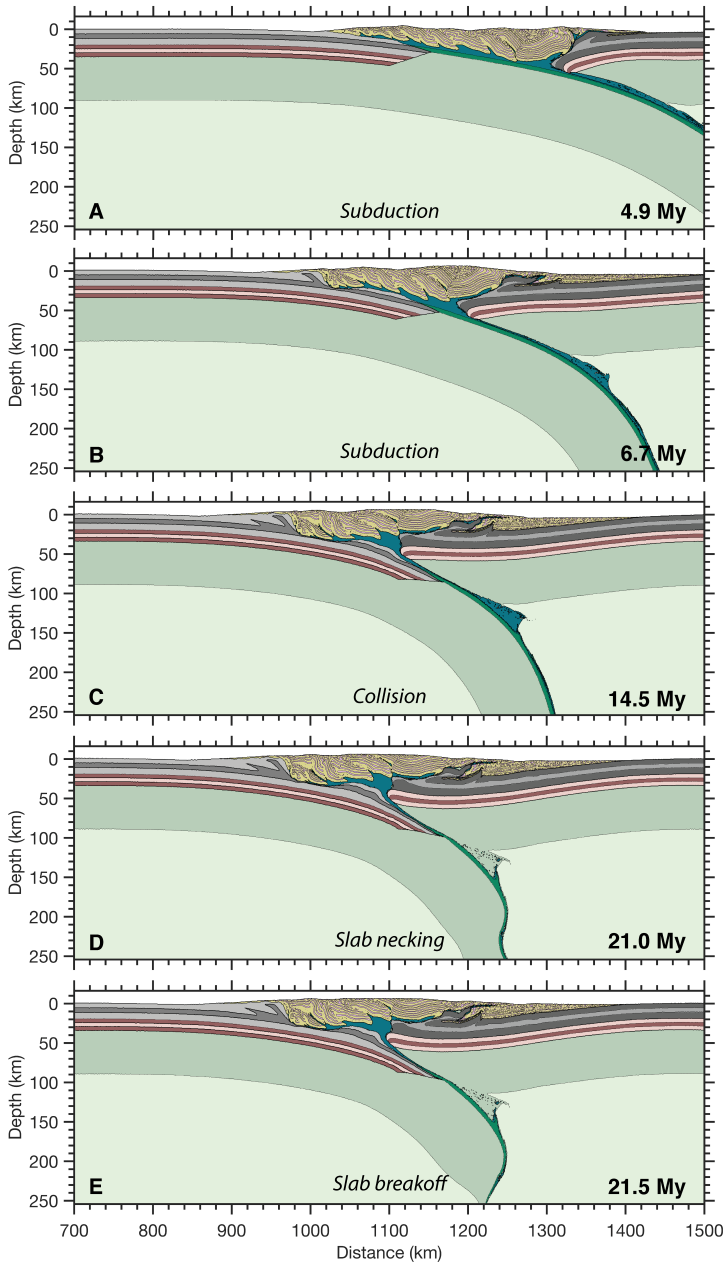

Figure 4: Long-term evolution of subduction (**A–B**), collision (**C**), slab necking (**D**), and slab breakoff (**E**). The early phases of the models consist of oceanic plate consumption and ocean closure. The collisional regime is greatly affected by the buoyant and rheologically weak materials entering the subduction channel from above. The final structure is that of a *coupled* collision system (e.g., Faccenda *et al.* , 2009).

development of retreating collision (Fig. 9). On the other hand, overthrusting of the orogenic wedge on the upper plate cause compressional stresses and, in turn, in a sequence of seismogenic thrusts at the front and beneath the retro-foreland basin (Fig. 8).

Deep earthquakes beneath the foreland basin extend into the lower crust and their distribution correlates well with the flexural bending of the downgoing plate. Flexural bending transfers stresses

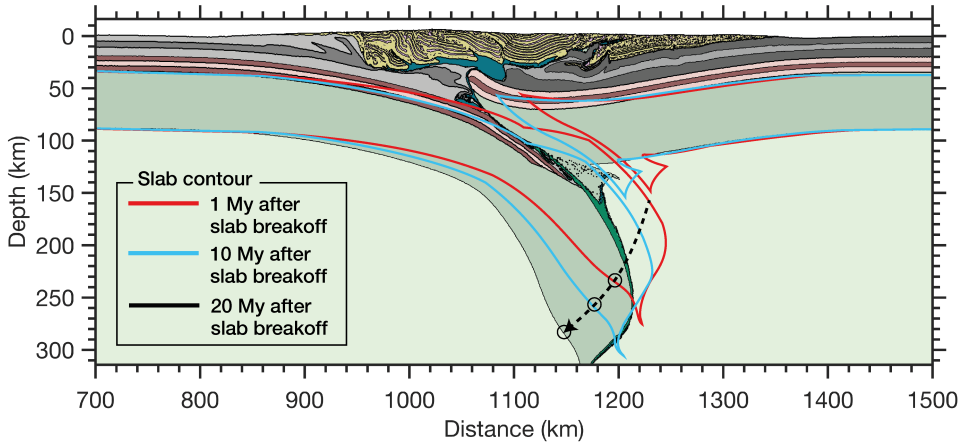

Figure 5: Post-collisional evolution with superimposed outlines of the slab geometries 1 and 10 My after slab breakoff. Compositional map shows the final structure 20 My after slab breakoff. Evolution of the orogen is driven by slow slab rollback and delamination of crustal material at all levels of lower plate.

into the lithosphere beneath the foreland basin and leads to a compressional component in the shallower domains and an extensional domain at deeper crustal levels (Fig. 8 and 9). The rheological differences between the lower crust and the brittle upper crust explain the peculiar rheological characteristics of the downgoing plate (Fig. 10). These results illustrate how the long-term tectonic evolution and crustal properties affect the architecture of the orogen and thereby their short-term spatial distribution of seismicity.

4. Discussion and Conclusions

Over the last decades, the evolution of the Alpine orogen has mainly been discussed in a kinematic framework (Handy *et al.* , 2010; Schmid *et al.* , 1996). This concept considers the kinematic relative movements between the colliding plates as the major driver of orogenesis, while the vertical forces — exerted by the buoyant crustal root and the subducted slab — have generally been neglected. In contrast, our study demonstrates that the dynamic forces, provided by a SRO model, can potentially explain the construction of an orogen with a pronounced topography and a stack of crustal material even in the absence of any convergence or of hard collision between two continental plates. Moreover, the kinematic concept based on the relative movements between the colliding plates is consistent neither with the current seismic regime nor with first-order isodynamic mass and force balancing approximations, which call for a different geodynamic model.

Our numerical experiments indicate that a rheologically "soft" collision regime facilitated by rollback mechanics can lead to the subduction of continental material. If the crust remains coupled to the downgoing slab, a large buoyancy force is generated. When these deep crustal domains are warmed up, they decouple from the downgoing slab and are subjected to buoyant extrusion and delamination. According to our results, the propagation of the foreland front, coeval with a pervasive crustal delamination — ductile at depth and brittle at shallower levels — suggest a predominant importance of the vertical slab load force. This is accomplished through a self-driven slab rollback,

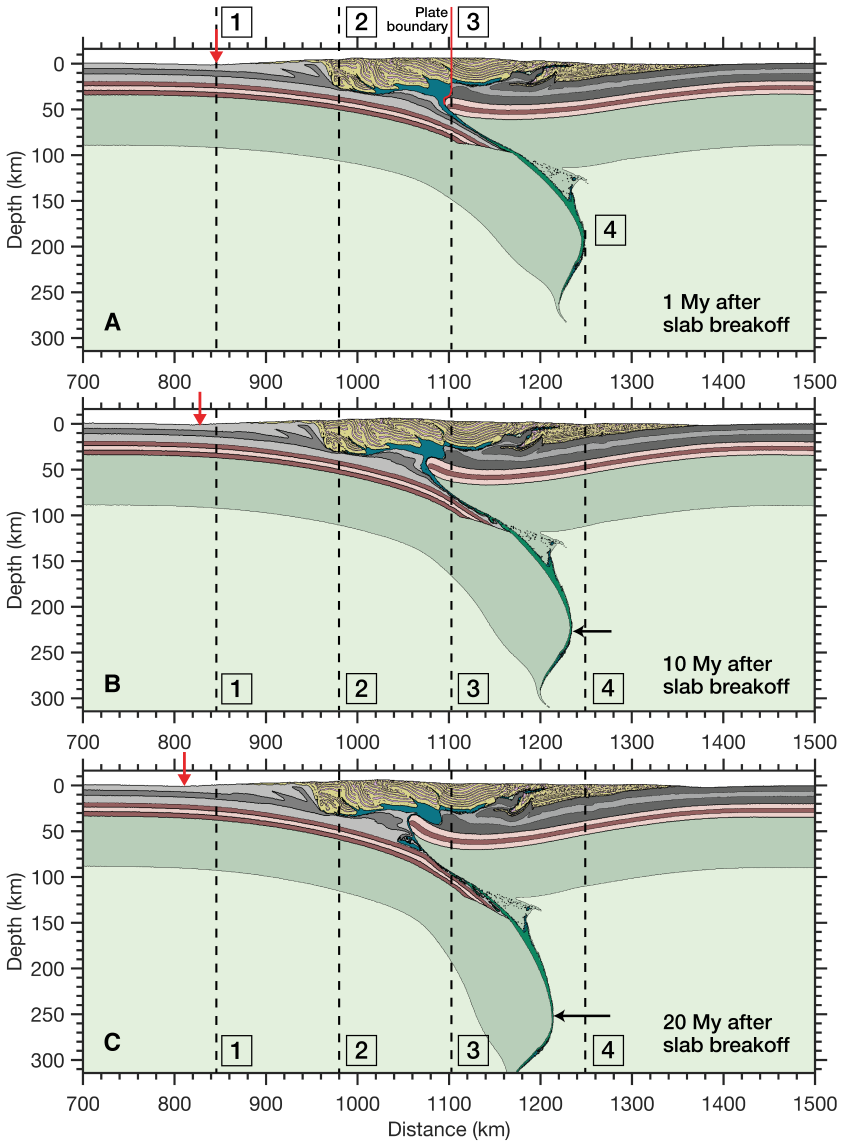

Figure 6: Post-collisional evolution at 1 My (**A**), 10 My (**B**), and 20 My (**C**) after slab breakoff. (**1**): Location of northern front of orogen at the surface. Red arrows indicate the position of the orogenic piedmont. (**2**): Location of northern edge of the accretionary wedge and the upper crust at 20 km depth; (**3**): Surface location of plate boundary (solid red line), (**4**): Position of the slab tip.

where the sinking rate of the slab is conditioned by the delamination of the crust from the mantle lithosphere as a consequence of bending-related extensional stresses, suction force, and heating of the deep crust. Most importantly, these processes create a positive feedback where delamination of buoyant crustal material from the subducting plate increases the relative importance of the vertical slab load, thus promoting further down warping of the plate. Also, this mechanism not only localizes the extensional stresses at the Moho but also within the crust, with the consequence of intra-crustal seismicity at both shallow and deep crustal levels. We also point out that the retreating collisional regime found in this SRO model is a distinct and dissimilar feature compared to previously

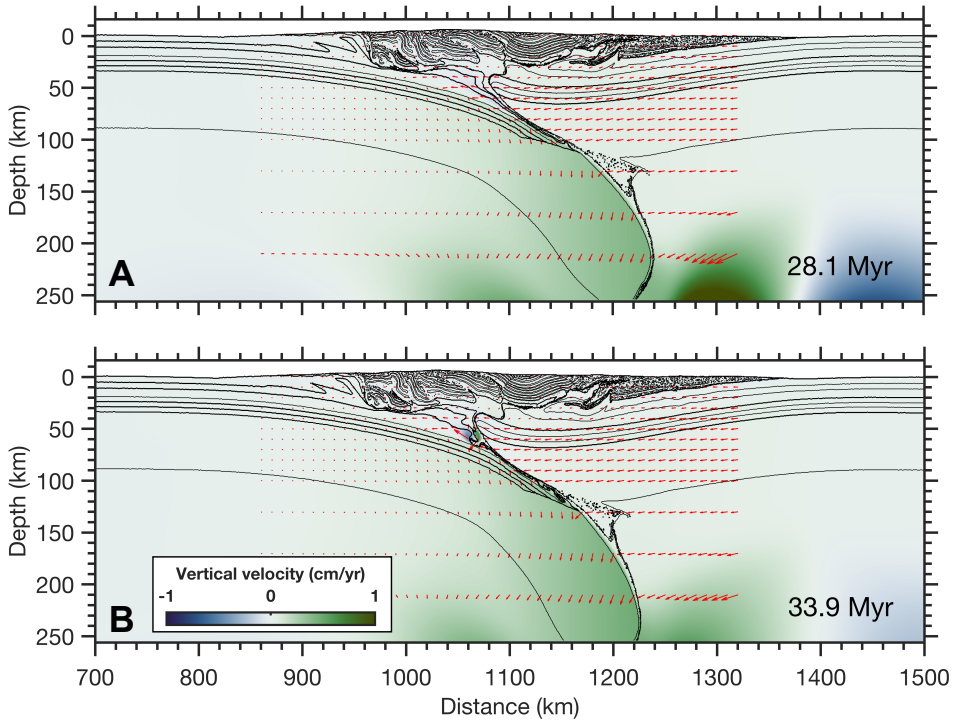

Figure 7: Vertical velocity field in color overlain by arrows indicating velocities at 28.1 (∼7 My after slab breakoff) and 33.9 (∼13 My after slab breakoff). The inferred velocity fields show how the vertical sinking of the post breakoff remaining slab translates into horizontal convergence of the upper plate and uplift in the core of the orogen.

investigated post-subduction collisional orogeny models, which are usually characterized by a fixed position of the overriding plate (e.g., Warren *et al.* , 2008; Faccenda *et al.* , 2009; van Hunen & Allen, 2011; Pusok *et al.* , 2018).

In natural convergent margins other aspects may play a relevant role, such as the three dimensionality or magmatism. Magmatism likely affects the distribution of the differential forces and is lacking in our numerical experiments (e.g., Menant *et al.* , 2016). Also, the lateral, third dimension is absent in our numerical model, which does not allow analyzing the role of transtensional/transpressional deformation (e.g., Magni *et al.* , 2017; Pusok *et al.* , 2018). However, while the direct application to the Alpine case may not be warranted at local smaller scale, slab rollback, crustal delamination, surface deformation, and post-orogenic reorganization should be consistent emerging features of interactions between large-scale geodynamic processes and shallow tectonic deformation, analogous to what we present here (Lister *et al.* , 2001; Brun & Faccenna, 2008).

Despite the along-strike variability of the Alpine belt, the results of this study have several important implications at the orogenic scale of the Central Alps. Based on our novel numerical experiments, supported by a chronological pattern of crustal deformation (Schlunegger & Kissling, 2015) and on seismic tomography (Fry *et al.* , 2010), we argue that a SRO model for the European Alps is capable to explain (1) the stacking of nappes, (2) the growth of the buoyant crustal root, (3) the evolution of the Molasse foreland basin, and (4) the current extensional seismicity pattern. This is

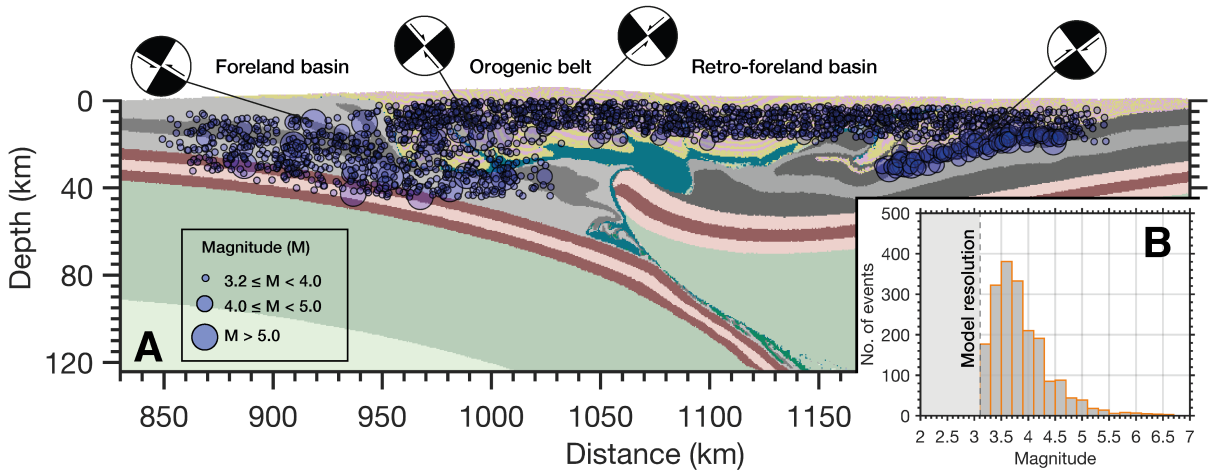

Figure 8: Short-term seismicity pattern of the reference model. **A**: Composition shows a broad orogen marked by nappe stacking in the core of the orogen, crustal delamination beneath the foreland basin and crustal shortening in the retro-foreland basin. The spatial evolution of seismicity and the inferred focal mechanisms display a broad pattern of different style of faulting, which are consistent with the local tectonic regime. **B**: Histograms of all events and the corresponding magnitude.

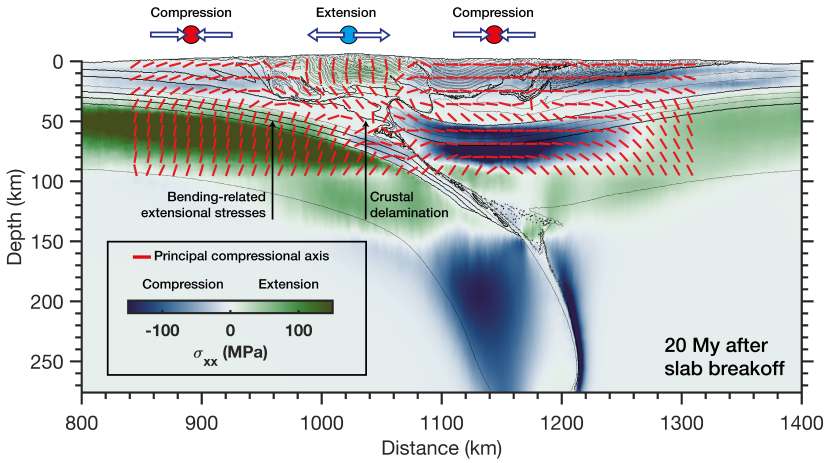

Figure 9: Analysis of the coupled collision reference model and rheological behavior of rocks at 41.5 My (20 My after slab breakoff). Color scale corresponds to the magnitude of normal stress (σ_{xx}). Red axes indicate orientations of maximum (compression) principal stresses. The inferred stress axes show a broad pattern of different tectonic regimes, which are consistent with the style of faulting and focal mechanisms shown in Fig. 8.

what we refer to as *Slab Rollback Orogeny* model and it contrasts with the previously published view on the collisional development of the Alps mainly because in our physics-based numerical model, crustal uplift, nappe stacking, and the buildup of topography are solely driven by ongoing rollback and conditioned by the mechanical strength of the subducting slab. In light of these results, while the Himalayas (e.g., Avouac, 2015a) and possibly the Andes (e.g., Oncken *et al.* , 2006) serve as much better examples where mountain building processes are driven by the horizontal push of the

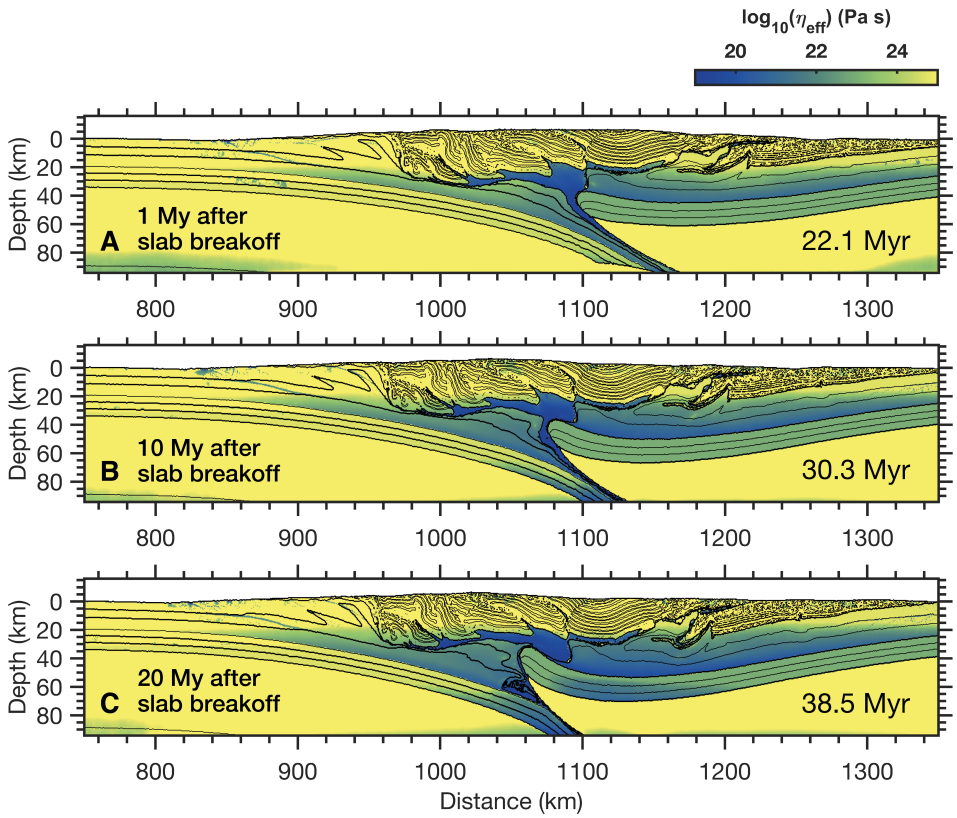

Figure 10: Viscosity field at 1 My (**A**), 10 My (**B**), and 20 My (**C**) after slab breakoff. The rheological differences between the deeper lower crust and the brittle high strength shallow crust illustrate how the long-term tectonic evolution and crustal properties affect the architecture of the orogen and thereby their short-term spatial distribution of seismicity.

subducting plate, the understanding of the geologic history of the Central Alps does require an alternative view.

Acknowledgements

This study was funded by the Swiss National Science Foundation Swiss Alp-Array SINERGIA and the Drinkward Fellowship at Caltech. Numerical simulations were performed on ETH cluster Euler. This paper benefited from discussions with Giacomo Pozzi, Kosuke Ueda, and Alberto Ceccato. Figures were made using perceptually uniform colormaps (Crameri, 2018).

References

Allmann, Bettina P, & Shearer, Peter M. 2009. Global variations of stress drop for moderate to large earthquakes. *Journal of Geophysical Research: Solid Earth*, **114**(B1).

Ampuero, J-P, & Ben-Zion, Y. 2008. Cracks, pulses and macroscopic asymmetry of dynamic rupture on a bimaterial interface with velocity-weakening friction. *Geophysical Journal International*, **173**(2), 674–692.

Avouac, Jean-Philippe. 2015a. Mountain building: From earthquakes to geologic deformation. *Treatise on Geophysics,*, **6**, 381–432.

Beaumont, Christopher, Ellis, Susan, Hamilton, Juliet, & Fullsack, Philippe. 1996. Mechanical model for subduction-collision tectonics of Alpine-type compressional orogens. *Geology*, **24**(8), 675–678.

Beller, S, Monteiller, V, Operto, S, Nolet, G, Paul, A, & Zhao, L. 2017. Lithospheric architecture of the South-Western Alps revealed by multiparameter teleseismic full-waveform inversion. *Geophysical Journal International*, **212**(2), 1369–1388.

Brun, Jean-Pierre, & Faccenna, Claudio. 2008. Exhumation of high-pressure rocks driven by slab rollback. *Earth and Planetary Science Letters*, **272**(1-2), 1–7.

Burkhard, Martin. 1990. Aspects of the large-scale Miocene deformation in the most external part of the Swiss Alps (sub-Alpine molasse to Jura fold belt). *Eclogae Geologicae Helvetiae*, **83**(3), 559–583.

Calais, E, Nocquet, J-M, Jouanne, F, & Tardy, M. 2002. Current strain regime in the Western Alps from continuous Global Positioning System measurements, 1996–2001. *Geology*, **30**(7), 651–654.

Crameri, F. 2018. *Scientific colour-maps*.

Crameri, F, Schmeling, H, Golabek, GJ, Duretz, T, Orendt, R, Buiter, SJH, May, DA, Kaus, BJP, Gerya, TV, & Tackley, PJ. 2012. A comparison of numerical surface topography calculations in geodynamic modelling: An evaluation of the 'sticky air'method. *Geophysical Journal International*, **189**(1), 38–54.

Dal Zilio, Luca. 2018. Subduction-driven Earth machine. *Nature Geoscience*, **11**(4), 229–229.

Dal Zilio, Luca, Faccenda, Manuele, & Capitanio, Fabio. 2018a. The role of deep subduction in supercontinent breakup. *Tectonophysics*, **746**, 312–324.

Dal Zilio, Luca, van Dinther, Ylona, Gerya, Taras V, & Pranger, Casper C. 2018b. Seismic behaviour of mountain belts controlled by plate convergence rate. *Earth and Planetary Science Letters*, **482**(1), 81–92.

Del Gaudio, P, Di Toro, G, Han, R, Hirose, T, Nielsen, S, Shimamoto, T, & Cavallo, A. 2009. Frictional melting of peridotite and seismic slip. *Journal of Geophysical Research: Solid Earth*, **114**(B6).

Den Hartog, SAM, Niemeijer, AR, & Spiers, CJ. 2012. New constraints on megathrust slip stability under subduction zone P–T conditions. *Earth and Planetary Science Letters*, **353**, 240–252.

Dewey, JF, Helman, ML, Knott, SD, Turco, E, & Hutton, DHW. 1989. Kinematics of the western Mediterranean. *Geological Society, London, Special Publications*, **45**(1), 265–283.

Di Toro, Giulio, Han, Raehee, Hirose, Takehiro, De Paola, Nicola, Nielsen, Stefan, Mizoguchi, Kazuo, Ferri, Fabio, Cocco, Massimo, & Shimamoto, Tosihiko. 2011. Fault lubrication during earthquakes. *Nature*, **471**(7339), 494–498.

Doin, Marie-Pierre, & Henry, Pierre. 2001. Subduction initiation and continental crust recycling: the roles of rheology and eclogitization. *Tectonophysics*, **342**(1-2), 163–191.

Duretz, Thibault, Gerya, Taras V, & May, Dave A. 2011. Numerical modelling of spontaneous slab breakoff and subsequent topographic response. *Tectonophysics*, **502**(1-2), 244–256.

Evans, Brian, & Goetze, Christopher. 1979. The temperature variation of hardness of olivine and its implication for polycrystalline yield stress. *Journal of Geophysical Research: Solid Earth*, **84**(B10), 5505–5524.

Faccenda, M, Minelli, G, & Gerya, TV. 2009. Coupled and decoupled regimes of continental collision: Numerical modeling. *Earth and Planetary Science Letters*, **278**(3-4), 337–349.

Faccenda, Manuele, & Dal Zilio, Luca. 2017. The role of solid–solid phase transitions in mantle convection. *Lithos*, **268**, 198–224.

Fox, Matthew, Herman, Frédéric, Kissling, Edi, & Willett, Sean D. 2015. Rapid exhumation in the Western Alps driven by slab detachment and glacial erosion. *Geology*, **43**(5), 379–382.

Fry, Bill, Deschamps, Frédéric, Kissling, Edi, Stehly, Laurent, & Giardini, Domenico. 2010. Layered azimuthal anisotropy of Rayleigh wave phase velocities in the European Alpine lithosphere inferred from ambient noise. *Earth and Planetary Science Letters*, **297**(1-2), 95–102.

Gerya, T. 2010. *Introduction to Numerical Geodynamic Modelling*. Cambridge University Press.

Gerya, Taras V, & Yuen, David A. 2007. Robust characteristics method for modelling multiphase visco-elasto-plastic thermo-mechanical problems. *Physics of the Earth and Planetary Interiors*, **163**(1), 83–105.

Gerya, Taras V, Yuen, David A, & Maresch, Walter V. 2004. Thermomechanical modelling of slab detachment. *Earth and Planetary Science Letters*, **226**(1-2), 101–116.

Handy, Mark R, Schmid, Stefan M, Bousquet, Romain, Kissling, Eduard, & Bernoulli, Daniel. 2010. Reconciling plate-tectonic reconstructions of Alpine Tethys with the geological–geophysical record of spreading and subduction in the Alps. *Earth-Science Reviews*, **102**(3-4), 121–158.

Ito, Keisuke, & Kennedy, George C. 1971. An experimental study of the basalt-garnet granulite-eclogite transition. *The structure and physical properties of the Earth's crust*, **14**, 303–314.

Kameyama, Masanori, Yuen, David A, & Karato, Shun-Ichiro. 1999. Thermal-mechanical effects of low-temperature plasticity (the Peierls mechanism) on the deformation of a viscoelastic shear zone. *Earth and Planetary Science Letters*, **168**(1-2), 159–172.

Karato, Shun-ichiro, Riedel, Michael R, & Yuen, David A. 2001. Rheological structure and deformation of subducted slabs in the mantle transition zone: implications for mantle circulation and deep earthquakes. *Physics of the Earth and Planetary Interiors*, **127**(1-4), 83–108.

Katayama, Ikuo, & Karato, Shun-ichiro. 2008. Low-temperature, high-stress deformation of olivine under water-saturated conditions. *Physics of the Earth and Planetary Interiors*, **168**(3), 125–133.

Kay, Robert W, & Kay, S Mahlburg. 1993. Delamination and delamination magmatism. *Tectonophysics*, **219**(1-3), 177–189.

Kissling, Edi. 1993. Deep structure of the Alps—what do we really know? *Physics of the Earth and Planetary Interiors*, **79**(1-2), 87–112.

Kissling, Edi, & Schlunegger, Fritz. 2018. Rollback orogeny model for the evolution of the Swiss Alps. *Tectonics*, **37**(4), 1097–1115.

Krystopowicz, Neil J, & Currie, Claire A. 2013. Crustal eclogitization and lithosphere delamination in orogens. *Earth and Planetary Science Letters*, **361**, 195–207.

Li, Zhong-Hai, Liu, Mian, & Gerya, Taras. 2016. Lithosphere delamination in continental collisional orogens: A systematic numerical study. *Journal of Geophysical Research: Solid Earth*, **121**(7), 5186–5211.

Lippitsch, Regina, Kissling, Edi, & Ansorge, Jörg. 2003. Upper mantle structure beneath the Alpine orogen from high-resolution teleseismic tomography. *Journal of Geophysical Research: Solid Earth*, **108**(B8).

Lister, GS, Forster, Margaret A, & Rawling, Timothy J. 2001. Episodicity during orogenesis. *Geological Society, London, Special Publications*, **184**(1), 89–113.

Lu, Gang, Kaus, Boris JP, & Zhao, Liang. 2011. Thermal localization as a potential mechanism to rift cratons. *Physics of the Earth and Planetary Interiors*, **186**(3-4), 125–137.

Magni, Valentina, Allen, Mark B, van Hunen, Jeroen, & Bouilhol, Pierre. 2017. Continental underplating after slab break-off. *Earth and Planetary Science Letters*, **474**, 59–67.

Malinverno, Alberto, & Ryan, William BF. 1986. Extension in the Tyrrhenian Sea and shortening in the Apennines as result of arc migration driven by sinking of the lithosphere. *Tectonics*, **5**(2), 227–245.

Menant, Armel, Sternai, Pietro, Jolivet, Laurent, Guillou-Frottier, Laurent, & Gerya, Taras. 2016. 3D numerical modeling of mantle flow, crustal dynamics and magma genesis associated with slab roll-back and tearing: The eastern Mediterranean case. *Earth and Planetary Science Letters*, **442**, 93–107.

Nikolaeva, K, Gerya, TV, & Marques, FO. 2010. Subduction initiation at passive margins: Numerical modeling. *Journal of Geophysical Research: Solid Earth (1978–2012)*, **115**(B3).

Oncken, Onno, Hindle, David, Kley, Jonas, Elger, Kirsten, Victor, Pia, & Schemmann, Kerstin. 2006. Deformation of the central Andean upper plate system—Facts, fiction, and constraints for plateau models. *Pages 3–27 of: The Andes*. Springer.

Platt, JP, Behrmann, JH, Cunningham, PC, Dewey, JF, Helman, M, Parish, M, Shepley, MG, Wallis, S, & Western, PJ. 1989. Kinematics of the Alpine arc and the motion history of Adria. *Nature*, **337**(6203), 158.

Prager, W, & Drucker, DC. 1952. Soil mechanics and plastic analysis or limit design, 0. *Appi. Math*, **10**(2), 157–165.

Pusok, Adina E, Kaus, Boris JP, & Popov, Anton A. 2018. The effect of rheological approximations in 3-D numerical simulations of subduction and collision. *Tectonophysics*, **746**, 296–311.

Ranalli, Giorgio. 1995. *Rheology of the Earth*. Springer.

Rudnick, Roberta L, & Fountain, David M. 1995. Nature and composition of the continental crust: a lower crustal perspective. *Reviews of geophysics*, **33**(3), 267–309.

Schlunegger, Fritz, & Kissling, Edi. 2015. Slab rollback orogeny in the Alps and evolution of the Swiss Molasse basin. *Nature communications*, **6**.

Schmid, Stefan M, Pfiffner, OA, Froitzheim, N, Schönborn, G, & Kissling, E. 1996. Geophysical-geological transect and tectonic evolution of the Swiss-Italian Alps. *Tectonics*, **15**(5), 1036–1064.

Schultz, RA. 1995. Limits on strength and deformation properties of jointed basaltic rock masses. *Rock Mechanics and Rock Engineering*, **28**(1), 1–15.

Seno, Tetsuzo. 2009. Determination of the pore fluid pressure ratio at seismogenic megathrusts in subduction zones: Implications for strength of asperities and Andean-type mountain building. *Journal of Geophysical Research: Solid Earth*, **114**(B5).

Sibson, Richard H. 1994. Crustal stress, faulting and fluid flow. *Geological Society, London, Special Publications*, **78**(1), 69–84.

Singer, J, Diehl, T, Husen, S, Kissling, E, & Duretz, T. 2014. Alpine lithosphere slab rollback causing lower crustal seismicity in northern foreland. *Earth and Planetary Science Letters*, **397**, 42–56.

Turcotte, D.L., & Schubert, G. 2002. *Geodynamics*. Cambridge University Press.

van Dinther, Y, Gerya, TV, Dalguer, LA, Mai, Paul Martin, Morra, G, & Giardini, D. 2013. The seismic cycle at subduction thrusts: Insights from seismo-thermo-mechanical models. *Journal of Geophysical Research: Solid Earth*, **118**(12), 6183–6202.

Van Heck, HJ, & Tackley, PJ. 2008. Planforms of self-consistently generated plates in 3D spherical geometry. *Geophysical Research Letters*, **35**(19).

van Hunen, Jeroen, & Allen, Mark B. 2011. Continental collision and slab break-off: a comparison of 3-D numerical models with observations. *Earth and Planetary Science Letters*, **302**(1-2), 27–37.

Warren, CJ, Beaumont, C, & Jamieson, Rebecca Anne. 2008. Modelling tectonic styles and ultra-high pressure (UHP) rock exhumation during the transition from oceanic subduction to continental collision. *Earth and Planetary Science Letters*, **267**(1-2), 129–145.

Wells, Donald L, & Coppersmith, Kevin J. 1994. New empirical relationships among magnitude, rupture length, rupture width, rupture area, and surface displacement. *Bulletin of the seismological Society of America*, **84**(4), 974–1002.

Willett, Sean D. 2010. Late Neogene erosion of the Alps: A climate driver? *Annual Review of Earth and Planetary Sciences*, **38**, 411–437.

Zhao, Liang, Paul, Anne, Guillot, Stéphane, Solarino, Stefano, Malusà, Marco G, Zheng, Tianyu, Aubert, Coralie, Salimbeni, Simone, Dumont, Thierry, Schwartz, Stéphane, *et al.* . 2015. First seismic evidence for continental subduction beneath the Western Alps. *Geology*, **43**(9), 815–818.

Zhao, Liang, Paul, Anne, Malusà, Marco G, Xu, Xiaobing, Zheng, Tianyu, Solarino, Stefano, Guillot, Stéphane, Schwartz, Stéphane, Dumont, Thierry, Salimbeni, Simone, *et al.* . 2016. Continuity of the Alpine slab unraveled by high-resolution P wave tomography. *Journal of Geophysical Research: Solid Earth*, **121**(12), 8720–8737.